

Two-photon-excited fluorescence spectroscopy of Rb atoms in a magneto-optical trap

Alan McLean¹, Christian Drago², Daniel Podos¹, Chengyi Luo¹,
 Caleb Brzezinski¹, Ting-Wei Hsu¹, John Sipe², and Ralph Jimenez^{1*}
 1. *JILA, 440 UCB, University of Colorado Boulder, Boulder, CO 80309, USA and*
 2. *University of Toronto, Department of Physics,
 60 St George St, Toronto, ON M5S 1A7, Canada*

We report the results of two-photon-excited fluorescence (TPEF) measurements of the $5S_{1/2} \rightarrow 5D_{1/2}$ transition of ^{85}Rb and ^{87}Rb cooled in a magneto-optical trap (MOT). We observe TPEF at excitation powers as low as $1 \mu\text{W}$ or fluxes as low as $4.30 \pm 0.22 \times 10^{18} \text{ photons cm}^{-2} \text{ s}^{-1}$ (^{85}Rb) and $5.17 \pm 0.26 \times 10^{18} \text{ photons cm}^{-2} \text{ s}^{-1}$ (^{87}Rb). Our results show that Rb, with additional benefits due to its ability to be optically cooled to the point where Doppler-broadening is negligible, is a promising platform for observing sensitive two-photon spectral signatures at low photon fluxes.

I. INTRODUCTION

Atomic rubidium (Rb) is of interest for optical clock [1, 2] and frequency standards [3, 4], matter wave interferometers and field sensors [5–8], and quantum simulation [9, 10], and is a resource for quantum computation [11]. Recently, Rb has gained attention as a medium suitable for probing the validity of entangled two-photon absorption (ETPA) [12–14]. ETPA occurs when an atom or molecule is driven by correlated photon pairs rather than classical light. The spectral-temporal correlations inherent in the two-photon state of light lead to a linear scaling of a nonlinear process. When compared to classical light, entangled photon pairs may provide a significant enhancement in the low intensity regime. Such an enhancement, if measurable, may be useful for applications relying on two-photon absorption, particularly where photodamage is of concern [15–17].

Despite significant interest from many research groups, a definitive detection of ETPA and enhancement due to ETPA has not been demonstrated. Some groups claim to detect ETPA with an enhancement many orders of magnitude above the classical result [18–25]. However, these results have been called into question by others who either do not measure an ETPA signal [26–28] or provide alternative explanations such as hot-band absorption or single-photon scattering for signals which first appear to be ETPA [29, 30]. Compared to recent experiments using molecular dyes, Rb offers a unique regime of parameter space that can be leveraged to increase the detection capabilities and therefore the measurement of ETPA.

For ETPA Rb is advantageous because the linewidths of atomic transitions are orders of magnitude smaller than the linewidths of electronic transitions of fluorescent dyes in room temperature solvents. In addition, as compared to other alkali atoms such as Li, Na, K, and Cs, though literature reports of their TPA cross-sections are scant, its two-photon detuning of 1.06 THz (2 nm, defined as the difference between the virtual state and the nearest

electronic state), is nearly 4-fold smaller than the second narrowest (Cs at 4.13 THz detuning), Appendix B. As a result the two-photon absorption (TPA) cross-section is on the order of 10^{12} GM ($1 \text{ GM} = 10^{-50} \text{ cm}^4 \text{ s photon}^{-1}$), which is approximately 8 orders of magnitude larger than the cross-section of molecular systems. This large TPA cross-section is of immense relevance for ETPA, as very low intensity is needed to witness an enhancement. Second, when pumped degenerately from the ground state ($5S_{1/2}$) to the two-photon excited state ($5D_{1/2}$) the first photon makes a transition near the 1.06 THz detuned real intermediate state, see Fig. 1. When compared to continuous wave classical light exciting a degenerate two-photon transition, the broadband nature of the ETPA photons from the SPDC process [31, 32] leads to spectral overlap and thus resonant excitation of the intermediate state increasing the excitation rate and therefore its quantum advantage [12].

For investigations of ETPA it is crucial that the system under review is well known and can be modeled so that one can accurately predict the results of experiments. For molecular systems this is often difficult as they are typically large complex molecules with many degrees of

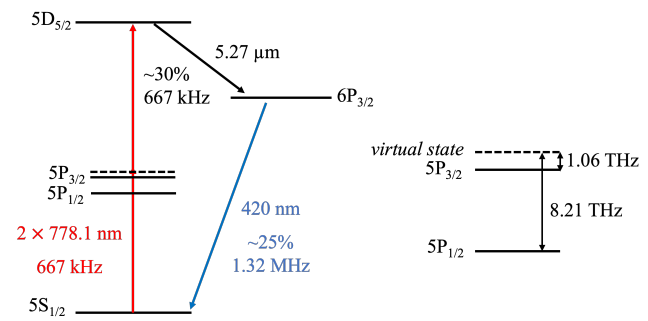


FIG. 1. The energy level diagram of the $5S_{1/2} \rightarrow 5D_{1/2}$ two-photon excitation of Rb (natural linewidth of 667 kHz). Branching ratios and radiative linewidths (calculated from the radiative lifetimes) [33] are reported. The narrow two-photon detuning (1.06 THz) between the virtual state and the nearest P state is depicted, in addition to the larger detuning (8.21 THz).

* Corresponding Author: rjimenez@jila.colorado.edu

freedom and where other physical mechanisms such as aggregation may be present. On the other hand, the properties of Rb are extremely well documented due to its many applications in quantum sensing [5, 6] and precision time and frequency calibrations [1–4]. Together these properties make Rb an ideal candidate for making nonlinear quantum-optic calculations.

Generally there are two types of experiments that are conducted with Rb atoms. Atoms can be in hot vapors cells or can be cooled in a magneto-optical trap (MOT). MOTs allow the confinement of millions atoms to a small region of space. With a focused excitation beam, this increases the detection capabilities of the experiment for lower incident powers as the rate of two-photon excitation increases quadratically with the photon flux.

Hot vapor systems suffer from Doppler broadening, effectively reducing the rate of excitation by 2-3 orders of magnitude with a classical beam as the bandwidth of light can be far less than the atomic linewidth. For classical TPA, a standard technique to circumvent the limitations due to Doppler broadening is to use counter propagating beams. On the other hand, photon pairs used for ETPA usually involve correlated degenerate photons with frequencies that add to the same value with a bandwidth much less than the natural linewidth. Consequently, ETPA is uniquely poised to be negatively effected by broadening mechanisms such as Doppler broadening [12]. Since the incident intensities are already very low, these effects may be large enough to suppress any measurable signal [12]. Further, unlike classical light where photons can be sent into counter propagating directions, one cannot “sort” correlated degenerate photons with equivalent polarizations as in Type-0 or Type-1 crystals such that the photons from a pair are counter propagating while maintaining the spectral-temporal correlations. Lastly, spectral shifts from Doppler broadening which could modulate the absorption rate [34] and “incoherent” two-photon absorption of the photon pairs [12] must be considered in hot vapors. These effects not only complicate the measurement, the incoherent two-photon absorption of the photon pairs could produce signatures such as in power dependence that mimics ETPA. In a MOT, however, the incoherent TPA rate is negligible due to the absence of substantive Doppler broadening [12].

To improve detection capabilities and remove the effects of Doppler broadening we present an analysis of Rb driven by classical TPA in a MOT cooled down to temperatures in the μK regime. Despite its potential, there are few reports of two-photon-excited fluorescence (TPEF) from ultracold Rb atoms [3, 4]. Previous works have reported TPEF of ultracold Rb down to 10 mW powers, which correspond to fluxes on the order of $10^{20} \text{ cm}^{-2} \text{ s}^{-1}$ [3, 4]. In this report, we demonstrate TPEF power-dependence of ultracold Rb down to excitation powers of $\sim 1 \mu\text{W}$ or fluxes as low as $4.30 \times 10^{18} \text{ cm}^{-2} \text{ s}^{-1}$. This sensitivity in flux is better than any previously published atomic two-photon study by over a factor of 10-fold, or a factor of >100 -fold in terms of counts, since the TPEF counts scale

quadratically with power. Additionally, this sensitivity is greater than the best molecular ETPA studies to-date as well by ~ 5 x [29]. Our results demonstrate that the Rb MOT is a promising platform for low-flux TPEF to be used for observing novel non-linear phenomena like ETPA.

The outline of this paper is as follows: In Sec. II we provide an outline of our procedure with results provided in Sec. III. Our concluding remarks are presented in Sec. IV with various supplementary information provided in appendices.

II. Experimental Overview

Here we provide an overview of our experiment (schematic shown in Figure 2). An Inflection mini-MOT V2 dispenses Rb (natural isotope abundance) at an ultralow pressure (nTorr) into a sealed, optically transparent glass cell. Taking advantage of the natural isotope composition, we created MOTs of both ^{85}Rb and ^{87}Rb . In brief, trap and repump diode lasers with frequencies either locked to ^{85}Rb and ^{87}Rb (see details in Appendix A-a) were sent into the MOT to optically cool and keep atoms in a single hyperfine ground state ($5S_{1/2} F_g = 3$ for ^{85}Rb , and $5S_{1/2} F_g = 2$ for ^{87}Rb). We used an optical chopper to activate and deactivate the trap and repump beams with a 50-50 duty cycle, providing a time window for probing the MOT when all atoms were in the ground state (when the beams were disengaged). This cycle produced a steady-state MOT. The number of trapped atoms in

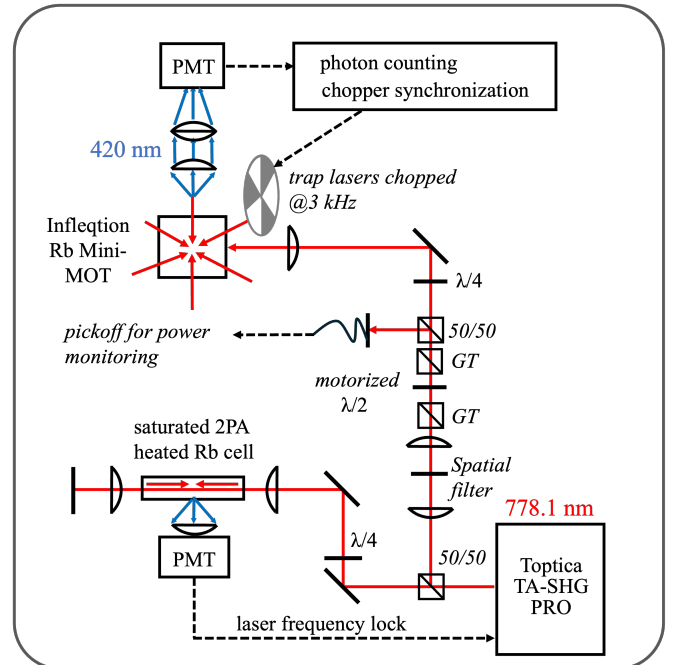


FIG. 2. Schematic for two-photon excitation of the Rb MOT. GT = Glan-Taylor polarizer.

the MOT was determined via absorption using a separate probe laser for imaging during the time window when the trap and repump beams were blocked (see Appendix A-d).

Two-photon excitation of the MOT was performed using a laser (778.1 nm) locked via Doppler-free two-photon spectroscopy to the strongest two-photon transition of each isotope ^{85}Rb ($5\text{S}_{1/2}, F_g = 3 \rightarrow 5\text{D}_{5/2}, F_f = 5$) and ^{87}Rb ($5\text{S}_{1/2}, F_g = 2 \rightarrow 5\text{D}_{5/2}, F_f = 4$). Using a motorized waveplate controller and Glan-Taylor polarizer, the power of the beam could be varied for power dependence studies. After the Glan-Taylor polarizer, a 50-50 beamsplitter was used as a pickoff to monitor the beam power, while the remainder of the beam was sent into the MOT. After the beamsplitter, a quarter-waveplate was used to create circularly polarized light. Fluorescence was collected orthogonally to the excitation using a custom-designed 2-lens system that focused light into a photon-counting PMT. The fluorescence signal was time-gated (synchronized with the optical chopper) to analyze data only when the trap and repump beams were blocked. The TPEF experiment was fully automated. To achieve optimal statistical averaging, low power points (where the signal-to-noise reaches the noise floor) were run for up to 4 hours (5 s on-off cycles). The averaging time was chosen by considering the Allan deviation measurements (Appendix E), because after 4 hours the Allan deviation deviated from linearity. Data processing was performed using hand-coded Python scripts for all measurements (two-photon power dependence studies, absorption imaging, etc.).

III. Results and discussion

Fluorescence collection methods are less prone to error, and can achieve higher sensitivities, than absorption approaches (as demonstrated by our group, up to a factor 10^3 to 10^4 better in the context of the two-photon cross-section) [35]. We thus utilized the two-photon excited fluorescence (TPEF) method [36] to determine the two-photon absorption cross-section of Rb. The TPEF method involves measuring the power-dependent fluorescence of the sample [36]. Power-dependent TPEF spectroscopy was performed on the trapped Rb atoms. For both ^{85}Rb and ^{87}Rb , the log-log plot of the power dependence had a slope of 2.0, within statistical significance, Figure 3. This indicates that the fluorescence originates purely from TPA.

Using the y-intercept values from the fit, and parameters from the experiment (such as the atom number, MOT dimensions, and beam waist; full parameters shown in Appendix D), the two-photon cross-section of each Rb isotope was calculated. For ^{85}Rb , the two-photon cross-section was $7.64 \pm 1.03 \times 10^{11}$ GM, Table I. 9.4% smaller (average), the ^{87}Rb two-photon absorption cross-section was $6.92 \pm 0.98 \times 10^{11}$ GM, Table I. Within error, the difference in two-photon cross-section between ^{85}Rb and ^{87}Rb closely matches theory (10.9% predicted) [37].

The two-photon cross-section measurement has four main sources of error: the log-log fit intercept, the spot size, the atom density, and the collection efficiency, Appendix D. The statistical uncertainty of the log-log fit is quantified by the 1σ uncertainty of the fitted y -intercept, yielding 6% for ^{85}Rb and 7% for ^{87}Rb . Fitting in log-space amplifies uncertainties (slopes are extracted with 0.2-0.4 % precision), and this error is small relative to the other parameters. For example, the focused spot size, calculated from the beam dimensions before the focus and taking into account the M^2 , has 10% error. The atom density also has $\sim 10\%$ error, which largely stems from error in determining the atom number (calculated via absorption imaging). Given the OD range of our experiment (up to ODs of 5), 10% error is expected [39] and would require advanced techniques to reduce further [40, 41]. Finally, the collection efficiency error (12.4%) is determined from Zemax modeling, Appendix G. We designed the fluorescence collection with 2 lenses to operate over wide offsets with minimal effect on the collection efficiency (Appendix G), and the error is comparable to other MOT experiments [42].

In addition to error sources, since the measured two-photon cross-section depends on the on-resonance fluorescence rate, it is important that the MOT two-photon excitation linewidth should be considered in interpreting the cross-section values. The observed two-photon linewidths in the MOT (1.5 ± 0.1 MHz, Appendix C) exceed its natural $5\text{D}_{5/2}$ linewidth of 667 kHz. This is

TABLE I. Experimental two-photon cross-sections in GM ($1 \text{ GM} = 10^{-50} \text{ cm}^4 \text{ s photon}^{-1}$) for Rb $5\text{S} \rightarrow 5\text{D}_{5/2}$. All reports in Table I used the two-photon excited fluorescence to determine the cross-section. Saha et al. and Zapka et al. used linearly polarized excitation in their studies. In this study, we used circular polarized excitation, which increases the two-photon excitation rate up to 1.75x. Detailed measurement parameters for our work are given in Table IV.

| Reference | Isotope | Method | δ (GM) |
|-------------------|------------------|-----------------------|-------------------------------------------------------------------------------------------------------|
| Saha et al. [37] | ^{85}Rb | Fiber linear pol. | 1.28×10^{12} |
| Zapka et al. [38] | ^{87}Rb | Hot vapor linear pol. | 1.0×10^{12} |
| <i>This work</i> | ^{85}Rb | MOT circular pol. | <i>measured</i> $7.64 \pm 1.45 \times 10^{11}$ <i>natural</i> $1.76 \pm 0.37 \times 10^{12}$ |
| <i>This work</i> | ^{87}Rb | MOT circular pol. | <i>measured</i> $6.92 \pm 1.38 \times 10^{11}$ <i>natural</i> $1.59 \pm 0.35 \times 10^{12}$ |

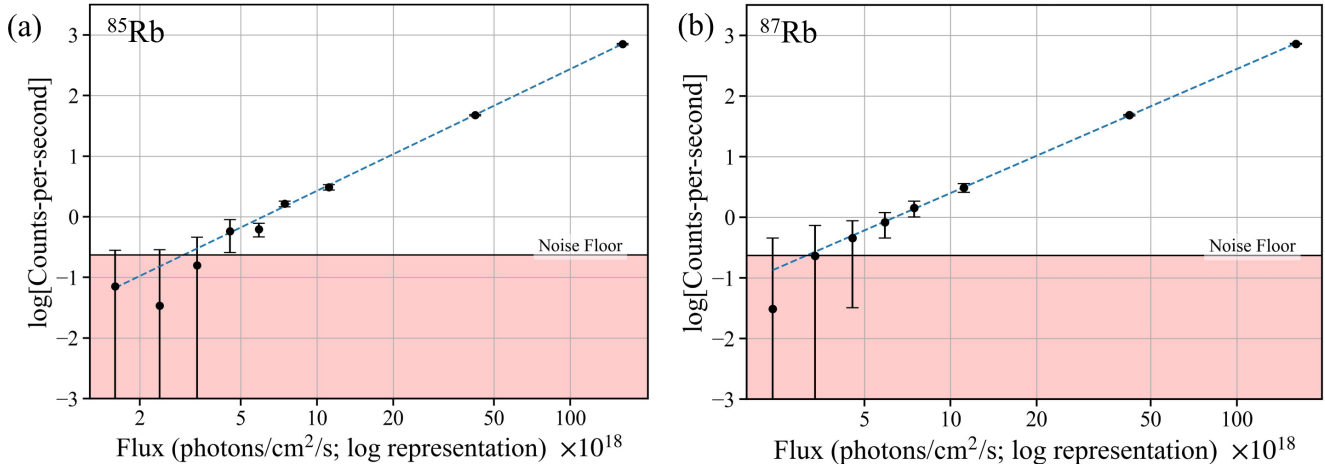


FIG. 3. Log-log power-dependence plots for (a) ^{85}Rb and (b) ^{87}Rb . Linear fits of the form $y = mx + b$ in \log_{10} - \log_{10} space give, for ^{85}Rb : $m = 2.009 \pm 0.004$, $b = -37.740 \pm 0.840$; and for ^{87}Rb : $m = 2.046 \pm 0.036$, $b = -38.466 \pm 0.699$. A slope consistent with $m \approx 2$ indicates fluorescence arising purely from two-photon processes. The noise floor is indicated by the solid black line; points whose error bars cross this line are not statistically significant.

likely due to magnetic-field effects that arise when the MOT coils remain on during the probe, of which we provide calculations in Appendix I. In this configuration the atoms occupy a distribution of magnetic sublevels m_F , each of which experiences a different Zeeman shift in the quadrupole magnetic field. Even within the small excitation volume set by the tightly focused 778 nm beam ($w_0 \approx 6.5 \mu\text{m}$, $z_R \approx 0.17 \text{ mm}$), the applied gradient of $\sim 14 \text{ G/cm}$ produces a field variation of order 0.2 G across the interaction region. When combined with the finite local field ($\sim 0.1\text{--}0.2 \text{ G}$), this leads to a corresponding multi-component Zeeman manifold in which different $m_F \rightarrow m_{F''}$ two-photon pathways are shifted by several hundred kilohertz relative to one another. Smaller contributions from residual Doppler broadening, pressure broadening, and power broadening also add in quadrature, but these effects are minor compared to the magnetic field-induced broadening, Appendix I.

Although the broadening would be dominated by inhomogeneous mechanisms, it is useful to estimate an effective TPA cross-section that would be inferred if the full linewidth were treated as homogeneous broadening of a single Lorentzian. Under that assumption the on-resonance response scales inversely with the linewidth, so rescaling from $\Gamma_{\text{MOT}} = 1.5 \pm 0.1 \text{ MHz}$ (Appendix C) to the natural 5D width $\Gamma_{\text{nat}} = 0.667 \text{ MHz}$ [33] multiplies the extracted cross-section by the factor $\Gamma_{\text{MOT}}/\Gamma_{\text{nat}} = 2.3 \pm 0.2$. Applying this factor with error propagation to our measured values yields natural-width upper limits $\delta_{85}^{(\text{nat})} \approx 1.76 \pm 0.37 \times 10^{12} \text{ GM}$ and $\delta_{87}^{(\text{nat})} \approx 1.59 \pm 0.35 \times 10^{12} \text{ GM}$, where these values should be interpreted as upper bounds, Table I.

To our knowledge, only two prior experimental studies have reported two-photon cross-sections for the same 5S \rightarrow 5D transitions in rubidium, both using linearly polarized excitation, Table I [37, 38]. Saha et al. report a value

of $\delta = 1.28 \times 10^{12} \text{ GM}$ for ^{85}Rb in a fiber-guided geometry, while Zapka et al. find $\delta \approx 1.0 \times 10^{12} \text{ GM}$ for ^{87}Rb in a vapor cell. Our MOT-based values, $7.64 \pm 1.03 \times 10^{11} \text{ GM}$ for ^{85}Rb and $6.92 \pm 0.98 \times 10^{11} \text{ GM}$ for ^{87}Rb , are smaller by roughly 30–40%. Both earlier works, however, employ analysis frameworks that normalize the extracted cross-section to the natural homogeneous linewidth (including transit-time and Doppler contributions in the fiber experiment), whereas our measurements reflects the linewidth present under MOT operating conditions. The natural linewidth two-photon cross-section estimates lie in the same 10^{12} GM range as these earlier ^{85}Rb and ^{87}Rb studies, Table I. Finally, we used circularly polarized excitation, which increases the two-photon excitation rate 1.75-fold [43], and would contribute to the higher cross-section bounds.

Having measured the two-photon cross-section of the cold Rb atoms, the sensitivity (the lowest power and fluxes to produce a signal with confidence factoring into account error) was determined. The power sensitivity of the measurement above the noise floor was $1.01 \mu\text{W}$ (^{85}Rb) and $1.21 \mu\text{W}$ (^{87}Rb) respectively, Table II. These limits are >100 x lower than was demonstrated in fiber [37], more than 1000x lower than has been demonstrated in alkali hot vapor [13], and more than 1000x lower than previously demonstrated in an ultracold MOT [3], Table II.

For ^{85}Rb and ^{87}Rb , the flux sensitivity was $4.30 \pm 0.22 \times 10^{18} \text{ photons cm}^{-2} \text{ s}^{-1}$ and $5.17 \pm 0.26 \times 10^{18} \text{ photons cm}^{-2} \text{ s}^{-1}$ respectively. When compared between previous Rb studies (Table II) and across ETPA studies [26, 29, 46], the sensitivity in flux is better than other previously published studies (for ETPA studies nearly 5x improved) [29]. While Rb density in the MOT ($2.22 \times 10^{10} \text{ cm}^{-3}$) is substantially lower than molecular systems (for example, a 1 mM molecular concentration corresponds to $6.02 \times 10^{17} \text{ cm}^{-3}$), the $>10^{10}$ larger cross-

TABLE II. Minimum detectable power P_{\min} and corresponding photon flux Φ_{\min} for atomic two-photon excitation experiments in Rb and Cs.

| Reference | Species | Platform | Type | P_{\min} | ϕ_{\min} (photons $\text{cm}^{-2} \text{ s}^{-1}$) |
|---------------------------|-------------------|------------------------|------------------|--------------------|-------------------------------------------------------------|
| Caracas Nunez et al. [37] | ^{133}Cs | Hot vapor fluorescence | power dependence | 10 mW | $1.63 \pm 0.11 \times 10^{22}$ |
| Saha et al. [37] | ^{85}Rb | Fiber fluorescence | power dependence | $200 \mu\text{W}$ | 7.8×10^{21} |
| Zapka et al. [38] | ^{87}Rb | Hot vapor fluorescence | operating | 60 mW | 1.6×10^{21} |
| Collins et al. [44] | ^{85}Rb | Hot vapor absorption | operating | 4.7 mW | $6.8 \pm 0.2 \times 10^{19}$ |
| Hassain et al. [45] | ^{87}Rb | Hot vapor IR emission | operating | 25 mW | 5.5×10^{20} |
| Leng et al. [3] | ^{87}Rb | MOT fluorescence | operating | 20 mW | - |
| <i>This work</i> | ^{85}Rb | MOT fluorescence | power dependence | $1.01 \mu\text{W}$ | $4.30 \pm 0.22 \times 10^{18}$ |
| <i>This work</i> | ^{87}Rb | MOT fluorescence | power dependence | $1.21 \mu\text{W}$ | $5.17 \pm 0.26 \times 10^{18}$ |

Notes: Saha *et al.* used two counter-propagating $100 \mu\text{W}$ beams (total = $200 \mu\text{W}$) in a hollow-core fiber [37]. Collins *et al.* used $P_+ = 2.9 \pm 0.1 \text{ mW}$ and $P_- = 1.8 \pm 0.1 \text{ mW}$ for each beam [44]. Lu et al. (2019) [4] (not included in table) published a study with same parameters as Leng *et al.* [3].

section pushes the measurement sensitivity into a new regime.

Our results indicate that ultracold Rb is a promising model platform for studying low-flux two-photon effects like ETPA. For example, using periodically-pooled KTP (ppKTP), we have produced up to 750 nW of SPDC when using a 389 nm seed (doubled from the 778.1 nm frequency-locked laser). This result, consistent with reports from literature, would produce a flux of 3.2×10^{18} photons $\text{cm}^{-2} \text{ s}^{-1}$ assuming an equivalent spot size to the classical beam. Using two SPDC crystals or double-passing SPDC photons through the MOT would push the flux above our limit of detection. In practice, however, focusing of a highly polychromatic source like SPDC is challenging (for example, at present, we have found we can focus the SPDC to $\sim 50 \mu\text{m}$). Future work is aimed to systematically study and optimize SPDC, and in tandem with theory, to measure an ETPA signal in the MOT platform.

IV. CONCLUSION

In conclusion, we studied two-photon excitation of Rb in a magneto-optical trap (MOT). Log-log power dependence studies confirmed fluorescence purely from two-photon absorption in the Rb MOT as indicated by the fitted slope of 2. We achieved $4.30 \pm 0.22 \times 10^{18}$ photons $\text{cm}^{-2} \text{ s}^{-1}$ (^{85}Rb) and $5.17 \pm 0.26 \times 10^{18}$ photons $\text{cm}^{-2} \text{ s}^{-1}$ (^{87}Rb) minimum flux sensitivity. With a flux sensitivity over an order of magnitude better than other published systems (and ~ 5 x

improved over deliberately optimized molecular ETPA studies), we find that ultracold Rb is a very promising platform for observing low-flux two-photon signatures.

ACKNOWLEDGMENTS

This work was supported by the NSF Physics Frontier Center at JILA (PHY 2317149) and the Natural Sciences and Engineering Research Council of Canada (NSERC). AM acknowledges support from the NRC research associateship programs (RAP), 2023-2025. We thank James Thompson for his advice in planning these experiments. We thank James Thompson and Adam Kaufman for feedback on the manuscript. AM thanks JILA electronics staff Terry Brown, Ivan Ryger, and James Fung-A-Fat, and all JILA machine shop staff. AM thanks Dr. Kristen Parzuchowski initiation at the start of his time at JILA and valuable discussions, and Miles San Soucie and Ryan Benson for help in the laboratory and valuable discussions.

Certain commercial equipment, instruments, or materials are identified in this paper in order to specify the experimental procedure adequately. Such identification is not intended to imply recommendation or endorsement by NIST, nor is it intended to imply that the materials or equipment identified are necessarily the best available for the purpose.

APPENDIX A. DETAILS OF EXPERIMENT

a. Cold Rb magneto-optical trap (MOT)

Using a standard six-beam geometry [47], we side-locked two near-infrared (NIR) lasers to the hyperfine transitions for cooling ($5S_{1/2} F = 3 \rightarrow 5P_{3/2} F' = 4$) and re-pumping ($5S_{1/2} F = 2 \rightarrow 5P_{3/2} F' = 3$) of ^{85}Rb , respectively. For ^{87}Rb , the corresponding cooling and re-pumping transitions are $5S_{1/2} F = 2 \rightarrow 5P_{3/2} F' = 3$ and $5S_{1/2} F = 1 \rightarrow 5P_{3/2} F' = 2$. The locking of both lasers was achieved using PII ('proportional-integral-integral') loop filters, and the MOT isotope (85 and 87) was readily selectable by tuning our lasers to the proper transitions.

In order to selectively excite ground-state Rb atoms (as when actively cooled the Rb atoms are optically driven between the $5S_{1/2}$ and $6P_{3/2}$ states), we employed an optical chopper set at 3 kHz to rapidly disengage and re-engage the cooling and re-pump lasers. With the optical chopper engaged, we trapped $>10^7$ atoms in a steady-state, which we quantified via absorption imaging of the MOT. By synchronizing the optical chopper with time-binned fluorescence detection (Hamamatsu H10682-210 PMT, PicoQuant HydraHarp 400), we probed the TPEF of the ultracold Rb atoms when all atoms were in the ground state, i.e. when the optical chopper was blocking the cooling and re-pump MOT beams.

b. Two-photon Excitation Source (Locked Standard)

In the ultracold MOT, Doppler-broadening is negligible, allowing for Doppler-free excitation of Rb. Frequency stabilization is thereby required in order to ensure that the laser used for two-photon excitation is on-resonance. Feedback control (peak locking) was used to maintain resonant laser excitation. To create the two-photon lock, we used a Toptica TA-SHG pro laser (778.1 nm emission) arranged in a Doppler-free configuration. We collected the TPEF using a two lens-filter-PMT design orthogonal to the hot Rb cell. The Rb cell was heated to $\approx 90^\circ\text{C}$.

Heating the Rb vapor cell increases the atomic density in the interaction region [48]. Temperatures of $\approx 90^\circ\text{C}$ are typically required to obtain a measurable signal [43, 49], whereas heating beyond $\sim 125^\circ\text{C}$ provides no further improvement in borosilicate cells and may gradually deplete the vapor through alkali-glass bonding [43, 50]. We therefore operated the cell only as hot as necessary for stable signal generation.

The cell was enclosed in a copper sheath with a side window for fluorescence collection. A 60 W silicone resistive heater was wrapped around the sheath and secured with worm-gear clamps. To prevent Rb condensation on the entrance and exit faces, custom copper end caps provided thermal contact to both windows, each containing a 2 mm beam aperture.

The assembly was supported by an Ultem cradle

mounted on a three-axis translation stage. Ultem, rated above 170°C [51], provides both mechanical rigidity and thermal isolation. Insulation performance was verified using 30 k Ω thermistors placed on the cell wall and within the cradle. After four hours at 50 W heater power, the cell stabilized at 140°C while the cradle remained within 1°C of ambient, confirming effective isolation.

The two-photon Doppler-free spectrum and associated error signals used for peak locking are shown in Figure 4. We achieved two-photon lock linewidths of <3.5 kHz (less than the linewidth of the laser grating) for ^{85}Rb and ^{87}Rb $5S_{1/2} \rightarrow 5D_{1/2}$ two-photon excitation. This lock stability enables probing of our MOT cloud without deviations off resonance.

c. Absolute two-photon cross-section

For a degenerate CW two-photon transition $|g\rangle \rightarrow |e\rangle$ at wavelength λ , the detected fluorescence count rate F

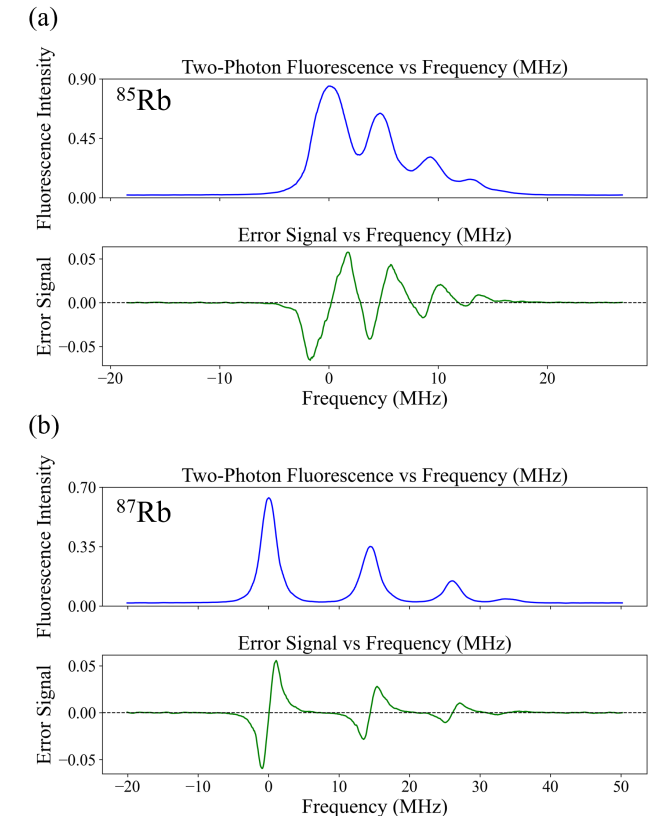


FIG. 4. (a) (Top) Two-photon Doppler-free spectrum of hot ^{85}Rb vapor (heated to $\approx 90^\circ\text{C}$). FWHM (the strongest hyperfine peak) is 3.8 MHz. (Bottom) Error signal (green) used for locking. The points at which the error signal is 0.00 (dashed line) represent potential lock points. (b) (Top) Two-photon Doppler-free spectrum in hot ^{87}Rb vapor (heated to $\approx 90^\circ\text{C}$). FWHM (the strongest hyperfine peak) is 2.4 MHz. (Bottom) corresponding error signal.

(s^{-1}) under weak excitation is

$$F = \eta B \frac{\delta}{(h\nu)^2} \int n(\mathbf{r}) I^2(\mathbf{r}) d^3\mathbf{r}, \quad (\text{A1})$$

where η is the total detection efficiency, B is the branching ratio for the detected channel, $\nu = c/\lambda$, $n(\mathbf{r})$ is the atomic number density, $I(\mathbf{r})$ is the irradiance, and δ is the (molecular/atomic) two-photon cross-section in GM units ($1 \text{ GM} \equiv 10^{-50} \text{ cm}^4 \text{ s photon}^{-1}$).

CW Gaussian beam

For a fundamental Gaussian beam of total power P and waist w_0 at the atoms,

$$I(r, z) = \frac{2P}{\pi w^2(z)} \exp\left(-\frac{2r^2}{w^2(z)}\right), \quad (\text{A2})$$

$$w(z) = w_0 \sqrt{1 + \left(\frac{z}{z_R}\right)^2}, \quad z_R = \frac{\pi w_0^2}{\lambda}.$$

If the cloud is large compared with w_0 transversely and extends over many Rayleigh ranges ($|z| \gg z_R$ where I^2 still contributes), we may take $n(\mathbf{r}) \approx n$ (constant) over the region where I^2 is non-negligible. Then

$$\int I^2(\mathbf{r}) d^3\mathbf{r} = \frac{P^2 z_R}{w_0^2}. \quad (\text{A3})$$

More generally, for a finite cloud between $z = z_1$ and $z = z_2$,

$$\int I^2(\mathbf{r}) d^3\mathbf{r} = \frac{P^2}{\pi} \int_{z_1}^{z_2} \frac{dz}{w^2(z)} = \frac{P^2 z_R}{\pi w_0^2} \left[\arctan\left(\frac{z}{z_R}\right) \right]_{z_1}^{z_2}. \quad (\text{A4})$$

If the cloud is Gaussian with FWHM sizes $\text{FWHM}_{x,y,z}$, one may approximate the density by a 3D Gaussian and evaluate $\int n I^2 dV$ as a product of 1D Gaussian integrals near the waist; for $\text{FWHM}_z \gg z_R$ it reduces back to Eq. (A3).

Solving for δ from a log-log power scan

Experimentally one fits $F = \alpha P_{\text{meas}}^2$ on a log-log plot (slope ≈ 2 confirms two-photon). Let $P_{\text{atoms}} = T P_{\text{meas}}$ be the power at the atoms after adjustments factoring into account beam-splitter ratio and losses, $T \approx 1.0254$, Table IV. Using Eqs. (A1) and (A3):

$$\alpha P_{\text{meas}}^2 = \eta B \frac{\delta}{(h\nu)^2} n \left(\frac{P_{\text{atoms}}^2 z_R}{w_0^2} \right), \quad (\text{A5})$$

$$\delta = \alpha \frac{(h\nu)^2}{\eta B n} \frac{w_0^2}{z_R} \frac{P_{\text{meas}}^2}{P_{\text{atoms}}^2}.$$

Here n is the number density. By measuring the total atom number N and assuming the cloud is near-uniform across the illuminated region, we substitute $n \simeq N/V_{\text{cloud}}$. For a 3D Gaussian atom cloud, $V_{\text{cloud}} = (\pi)^{3/2} \sigma_x \sigma_y \sigma_z$, with $\sigma = \text{FWHM}/(2\sqrt{2 \ln 2})$. We also use the beam size conversions: $w_0 = \text{FWHM}_{\text{beam}}/\sqrt{2 \ln 2}$.

Minimum statistically significant excitation power and flux

In a log-log excitation scan the measured fluorescence is converted to $y = \log_{10} F$ and plotted versus either $x = \log_{10} P_{\text{meas}}$ or, after correcting for the beam geometry, $x = \log_{10} \Phi$, where Φ is the photon flux at the atoms. Only data points whose measured count rates lie above the experimentally determined noise floor are included in the linear regression, but the noise characteristics of *all* data points (including those below the noise floor) are used in determining the detection limit.

Over the region used for fitting, the two-photon response is well described by the weighted linear model

$$y(x) = mx + b, \quad (\text{A6})$$

with parameter covariance

$$\Sigma = \begin{pmatrix} \sigma_m^2 & \text{Cov}(m, b) \\ \text{Cov}(m, b) & \sigma_b^2 \end{pmatrix}. \quad (\text{A7})$$

The 1σ uncertainty of the fitted line follows from standard error propagation. With

$$\mathbf{g}(x) = \begin{pmatrix} \partial y / \partial m \\ \partial y / \partial b \end{pmatrix} = \begin{pmatrix} x \\ 1 \end{pmatrix},$$

the variance of the fitted mean is

$$\sigma_{\text{fit}}^2(x) = \mathbf{g}(x)^T \Sigma \mathbf{g}(x) = x^2 \sigma_m^2 + \sigma_b^2 + 2x \text{Cov}(m, b). \quad (\text{A8})$$

Measurement noise, which grows rapidly as the fluorescence approaches the noise floor, contributes an additional term $\sigma_{\text{data}}(x)$. The total 1σ predictive uncertainty at excitation level x is

$$\sigma_{\text{pred}}(x) = \sqrt{\sigma_{\text{fit}}^2(x) + \sigma_{\text{data}}^2(x)}. \quad (\text{A9})$$

Let y_{noise} denote the measured noise-floor level in log space. The minimum statistically significant excitation is defined as the smallest x for which the lower edge of the prediction band exceeds the noise floor:

$$y(x_{\text{det}}) - \sigma_{\text{pred}}(x_{\text{det}}) = y_{\text{noise}}. \quad (\text{A10})$$

Equation (A10) is solved numerically using a bracketing root-finding method. Because the interpolation $\sigma_{\text{data}}(x)$ incorporates all measured points, including those below the noise floor, no additional constraint is required on the location of x_{det} .

Finally, the minimum statistically significant excitation levels in physical units are

$$P_{\text{det}} = 10^{x_{\text{det}}^{(P)}}, \quad \Phi_{\text{det}} = 10^{x_{\text{det}}^{(\Phi)}}, \quad (\text{A11})$$

which represent the lowest excitation levels at which the two-photon signal is distinguishable from the noise floor at the 1σ confidence level.

d. Absorption Imaging

Frequency Stabilization and Sweeping

Absorption imaging was performed using a probe laser (a separate laser) that was frequency stabilized to the trap laser transition for absorption imaging by frequency offset locking (FOL), see reference for a general FOL scheme [52]. In brief, the repump laser was locked to its atomic transition via side-locking. Then, using polarization beam-splitters, the re-pump laser and the probe laser were combined using a 50/50 beamsplitter cube (one laser sent through each face). The polarizations of the repump and probe laser were set to be the same in order to ensure proper mixing [52]. The mixed lasers were fiber-coupled and sent for detection (Vescent D2 Beat Note Detector), with a difference in frequency on the order of 2.8–2.9 GHz. The GHz beat note was sent into a high frequency divider chip (ADF4007), and divided down into the MHz regime (by a factor of 64), for comparison to a reference (TPI 1005 synthesizer). The output of the ADF4007 chip was sent into a loop filter. By adjusting the reference frequency (synthesizer reference), the frequency offset was adjusted around the Rb trap transition.

Our absorption imaging scheme was inspired by other literature [53]. In brief, our probe laser was spatially filtered and optically chopped out of phase with our MOT trap and repump lasers. The probe laser was then directed through the MOT and imaged on a camera.

Optical Density Fitting

Absorption model with fixed natural linewidth

After normalizing the data, we model the transmitted intensity under the Beer–Lambert law with a Lorentzian line shape of fixed half-width half-max (HWHM) γ (in MHz). We use $\gamma = 6.06$ MHz and introduce a small phenomenological asymmetry parameter s to account for residual skew in the line:

$$I_{\text{model}}(\omega; \boldsymbol{\theta}) = a + \exp[-\text{OD} \mathcal{L}(\omega; \omega_0, s)], \quad (\text{A12})$$

$$\mathcal{L}(\omega; \omega_0, s) = \frac{\gamma^2}{4(\omega - \omega_0)^2 + s(\omega - \omega_0) + \gamma^2}. \quad (\text{A13})$$

Here $\boldsymbol{\theta} = (\text{OD}, \omega_0, a, s)$, where OD is the on-resonance optical density, ω_0 is the line center (in MHz), $a \in [0, 1]$ is a constant offset, and s controls weak asymmetry ($s = 0$ recovers the symmetric Lorentzian). We use s purely as a nuisance parameter to absorb mild nonidealities (e.g. residual gradients or detuning asymmetries).

Nonlinear least squares fit and constraints

For each pixel (r, c) we minimize the residual sum of squares

$$\min_{\boldsymbol{\theta}} \text{RSS}(\boldsymbol{\theta}) = \sum_{i \in \mathcal{K}} [I_{\text{model}}(\omega_i; \boldsymbol{\theta}) - \hat{y}_i(r, c)]^2, \quad (\text{A14})$$

over the index set \mathcal{K} remaining after filtering and trimming. We impose simple box constraints reflecting the

acquisition and normalization:

$$\begin{aligned} 0 \leq \text{OD} \leq 50, \quad \min_i \omega_i \leq \omega_0 \leq \max_i \omega_i, \\ 0 \leq a \leq 1, \quad -100 \leq s \leq 100. \end{aligned} \quad (\text{A15})$$

Goodness of fit and acceptance criterion

We report the coefficient of determination

$$R^2 = 1 - \frac{\sum_{i \in \mathcal{K}} (\hat{y}_i - \hat{y}_i^{\text{fit}})^2}{\sum_{i \in \mathcal{K}} (\hat{y}_i - \bar{y})^2}, \quad \bar{y} = \frac{1}{|\mathcal{K}|} \sum_{i \in \mathcal{K}} \hat{y}_i, \quad (\text{A16})$$

where $\hat{y}_i^{\text{fit}} = I_{\text{model}}(\omega_i; \hat{\boldsymbol{\theta}})$. If the denominator in Eq. (A16) vanishes we set $R^2 = -1$. Fits with $R^2 < 0.70$ are rejected by assigning $\widehat{\text{OD}} = 0$.

Optical density map

We assemble the per-pixel estimate $\widehat{\text{OD}}(r, c)$ into a 2D map of size $H \times W$ matching the input images. For a user-specified single pixel (r^*, c^*) , we can additionally plot the data and best-fit $\{\omega_i, \hat{y}_i(r^*, c^*)\}$ together with $I_{\text{model}}(\omega; \hat{\boldsymbol{\theta}})$ for evaluation (such as in Figure 5B and Figure 5C). All fits use bound-constrained nonlinear least squares (Levenberg–Marquardt-type) as implemented in `least_squares`.

Per-pixel uncertainty

For each pixel fit, the nonlinear least-squares routine (`least_squares`) returns the Jacobian J of the residuals with respect to the parameters, evaluated at the best-fit $\hat{\boldsymbol{\theta}} = (\widehat{\text{OD}}, \hat{\omega}_0, \hat{a}, \hat{s})$. Let $r_i(\hat{\boldsymbol{\theta}})$ denote the residual at frequency ω_i , and define the residual sum of squares

$$\text{RSS}(\hat{\boldsymbol{\theta}}) = \sum_{i \in \mathcal{K}} r_i(\hat{\boldsymbol{\theta}})^2. \quad (\text{A17})$$

With $N = |\mathcal{K}|$ data points and $P = 4$ fit parameters, we determine the noise variance as

$$\sigma^2 = \frac{\text{RSS}(\hat{\boldsymbol{\theta}})}{N - P}. \quad (\text{A18})$$

The parameter covariance matrix is then approximated by the usual Gauss–Newton expression

$$\Sigma_{\hat{\boldsymbol{\theta}}} = \sigma^2 (J^T J)^{-1}. \quad (\text{A19})$$

We take the on-resonance optical-density uncertainty for that pixel to be the square root of the corresponding diagonal element,

$$\delta\text{OD} = \sqrt{\Sigma_{\hat{\boldsymbol{\theta}}, 11}}, \quad (\text{A20})$$

where index 1 refers to the OD parameter in $\boldsymbol{\theta} = (\text{OD}, \omega_0, a, s)$. This “fit-based” 1σ uncertainty incorporates photon shot noise, camera noise, and any residual model mismatch that appears as scatter in the normalized intensity. The per-pixel uncertainties $\delta\text{OD}(r, c)$ are stored

in a map of the same size as $\widehat{\text{OD}}(r, c)$ and are used to propagate errors to the total atom number. Pixels with $R^2 < 0.70$ are assigned $\widehat{\text{OD}} = 0$ but retain their formal δOD in the error budget, so they contribute only to the uncertainty and not to the mean atom number.

Total atom number

The total atom number N is obtained by summing the optical density over all pixels and converting to atom number using the resonant scattering cross section,

$$N = \frac{A_{\text{pixel}}}{\sigma_0} \sum_{r,c} \widehat{\text{OD}}(r, c), \quad \sigma_0 = \frac{3\lambda^2}{2\pi}, \quad (\text{A21})$$

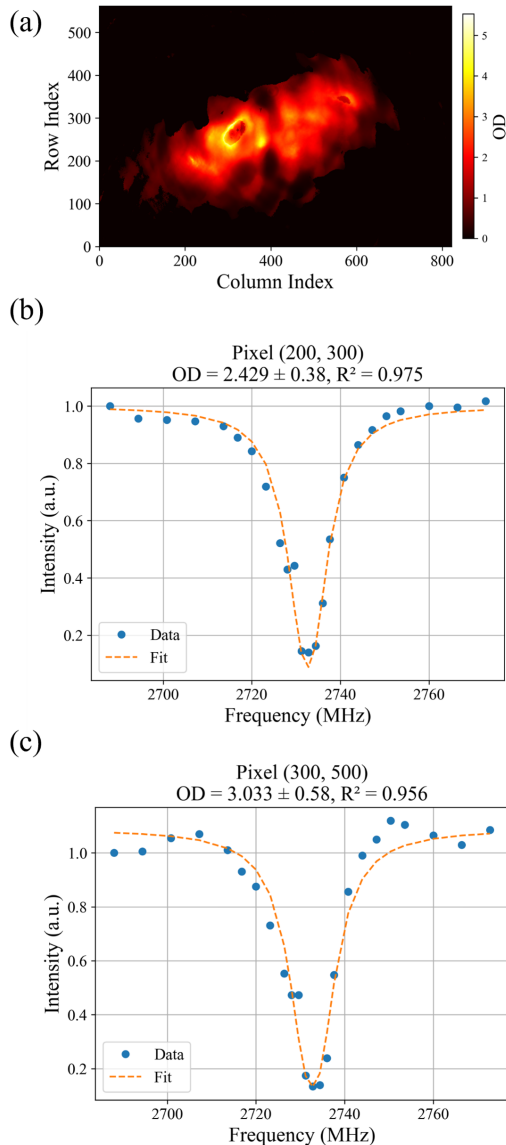


FIG. 5. (a) MOT absorption image with OD plotted as an intensity surface plot. (b-c) Fitting of example pixels used to produce the absorption OD plot (OD reported at the top of each figure, data shown in blue, fit shown in orange).

where A_{pixel} is the effective pixel area in the object plane (camera pixel area divided by the square of the imaging magnification) and λ is the imaging wavelength. In the analysis code we implement Eq. (A21) using a scale factor $\text{scale} = A_{\text{pixel}}/\sigma_0$.

Assuming that the per-pixel OD estimates are statistically independent, the variance of the summed OD is

$$\text{Var}\left[\sum_{r,c} \widehat{\text{OD}}(r, c)\right] = \sum_{r,c} \delta\text{OD}(r, c)^2, \quad (\text{A22})$$

so that

$$\text{Var}[N] = \left(\frac{A_{\text{pixel}}}{\sigma_0}\right)^2 \sum_{r,c} \delta\text{OD}(r, c)^2. \quad (\text{A23})$$

We therefore quote

$$N = N_{\text{est}} \pm \delta N, \quad \delta N = \frac{A_{\text{pixel}}}{\sigma_0} \sqrt{\sum_{r,c} \delta\text{OD}(r, c)^2}, \quad (\text{A24})$$

as the 1σ statistical uncertainty on the atom number inferred from the absorption image.

APPENDIX B. TWO-PHOTON DETUNINGS

The following table reports two-photon detunings for various alkali atoms (Li, Na, K, Rb, and Cs).

TABLE III. Degenerate two-photon wavelengths and detunings of the virtual state from the nearest real state for Li, Na, K, Rb, and Cs. The Rb two-photon transition studied in this manuscript is in bold.

| Atom | Transition | λ (nm) | Detuning (THz) |
|--------------------|-----------------------------------------------------|----------------|----------------|
| Li [54, 55] | $2\text{S} \rightarrow 4\text{S}$ | 571.3 | +33.6 |
| Li [56, 57] | $2\text{S} \rightarrow 3\text{D}$ | 639.1 | -22.7 |
| Na [58] | $3\text{S} \rightarrow 5\text{S}$ | 602.2 | +9.6 |
| Na [59] | $4\text{S} \rightarrow 4\text{D}$ | 578.7 | -10.5 |
| K [60] | $4\text{S} \rightarrow 6\text{S}$ | 728.4 | +22.3 |
| K [60] | $4\text{S} \rightarrow 4\text{D}$ | 730.0 | +19.7 |
| Rb [61–63] | $5\text{S} \rightarrow 7\text{S}$ | 760.0 | +10.2 |
| Rb [37, 38] | $5\text{S} \rightarrow 5\text{D}$ | 778.1 | +1.06 |
| Cs [13] | $6\text{S} \rightarrow 8\text{S}$ | 822.2 | +13.0 |
| Cs [64] | $6\text{S} \rightarrow 6\text{D}$ | 883.7 | +4.13 |

APPENDIX C. TWO-PHOTON EXCITATION LINETHICKNESSES AND OPTICAL CHOPPING

To excite the ultracold Rb MOT via two-photon excitation, the trap and repump beams must be blocked. If an optical chopper is not used, a significant portion of the atom population will be in the $5P_{3/2}$ state. From a theoretical standpoint, this is not ideal for modeling of the two-photon transition (although basic models incorporating the occupied $5P_{3/2}$ state have been considered for metrological applications) [3]. In addition, with the trap and repump beams engaged, line-broadening (by a factor

of $>250\%$) is observed, as shown in Figure 6A with the ^{87}Rb isotope studied. In the case of using full-power trap and repump beams, in the absence of optical chopping, a 4.0 MHz linewidth is observed (Figure 6B).

As discussed for the two-photon transitions of Li [65, 66] and Cs [64] atoms cooled via MOT, broadening when the cooling beams are engaged is due to power-broadening from the cooling lasers. This is proven by attenuating the cooling laser power (Figure 6C). At 90% attenuation a single Lorentzian that matches the linewidth with the cooling beams blocked is observed. For the main experiments in this paper (i.e. Figure 3), the two-photon excitation is time-gated and the data is analyzed only when the cooling beams are blocked.

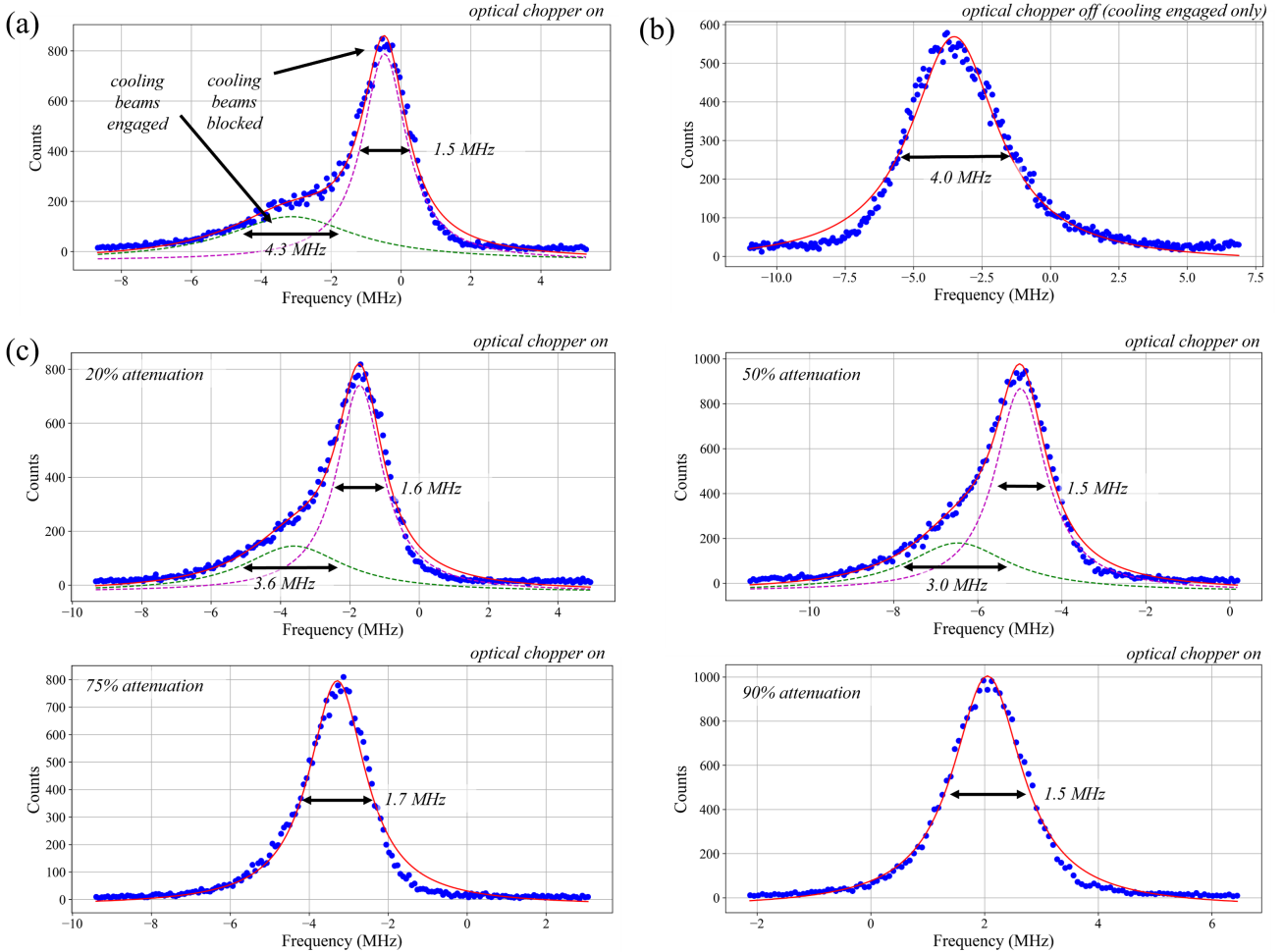


FIG. 6. MOT excitation spectra for various conditions, (a) Excitation spectra under full trap and repump power (optical chopper engaged), (b) Excitation spectra under full trap and repump power (optical chopper disengaged, therefore only the power broadening component exists), (c) Excitation spectra under attenuated trap and repump powers (optical chopper engaged).

APPENDIX D. FULL LIST OF TWO-PHOTON PARAMETERS TO CALCULATE THE CROSS-SECTION

TABLE IV. Quantities required to obtain the TPA cross-sections for ^{85}Rb and ^{87}Rb . Excitation-power correction uses the measured chain: beamsplitter mismatch, pre-cell optics, and a single glass face. Uncertainty budgets for δ combine (in quadrature) detection efficiency, atom number, fit-intercept, and beam-size contributions: ^{85}Rb (12.4%, 8.5%, 5.8%, 10.0%) \Rightarrow 18.6%; ^{87}Rb (12.4%, 9.5%, 7.1%, 10.0%) \Rightarrow 19.9%.

| Parameter | Symbol | Value |
|-----------------------------------------------------------------------------|--------------------------------------|--------------------------------------------------------------------------------------------------------------------------------|
| <i>Beam / Mode (common to both isotopes)</i> | | |
| Beam FWHM at focus | FWHM | $7.64 \pm 0.19 \mu\text{m}$ |
| Beam waist radius | w_0 | $6.49 \pm 0.16 \mu\text{m} (= 6.489 \times 10^{-4} \text{ cm})$ |
| Rayleigh length | z_R | $0.170 \pm 0.009 \text{ mm}$ |
| <i>Detection / Throughput (common)</i> | | |
| Overall detection efficiency | η | 0.0426 ± 0.0053 |
| PMT quantum efficiency | η_{PMT} | 0.284 |
| Collection optics efficiency | η_{optics} | 0.161 ± 0.020 |
| Fluorescence filters (96% & 97%) | η_{filters} | $0.96 \times 0.97 = 0.9312$ |
| Branching ratio to detected line | B | 0.08 (5D \rightarrow 6P _{3/2} \sim 30%; 6P _{3/2} \rightarrow 5S _{1/2} 420 nm \sim 25%) [33] |
| <i>Excitation Power Path (meter \rightarrow atoms, common)</i> | | |
| Beamsplitter mismatch | S_{split} | $210.6/191.0 = 1.1026$ |
| Pre-cell optics | T_{opt} | $201.5/210.6 = 0.9568$ |
| Single glass face (circular pol.) | T_{win} | 0.972 |
| Net transmission | T_{total} | $S_{\text{split}} T_{\text{opt}} T_{\text{win}} = 1.0254$ |
| Input-loss correction (excitation) | corr | $\alpha \rightarrow \alpha/1.0515$ |
| ^{85}Rb (TPA measurement) | | |
| Total atom number | N | $(1.37 \pm 0.12) \times 10^7$ |
| Cloud FWHM (x, y, z) | FWHM _{x, y, z} | (1.768, 0.4624, 0.6256) mm |
| Peak density | n_0 | $(2.22 \pm 0.19) \times 10^{10} \text{ cm}^{-3}$ |
| Free fit (base-10 logs) | m, b | $m = 2.009 \pm 0.004, b = -0.271 \pm 0.025$ |
| Fitted rate prefactor (corrected) | α_{corr} | $2.60 \times 10^{11} \text{ s}^{-1} \text{ W}^{-2}$ |
| Two-photon cross-section | δ | $(7.64 \pm 1.45) \times 10^{-39} \text{ cm}^4 \cdot \text{s}/\text{photon}$ $(7.64 \pm 1.45) \times 10^{11} \text{ GM}$ |
| ^{87}Rb (TPA measurement) | | |
| Total atom number | N | $(7.02 \pm 0.67) \times 10^6$ |
| Cloud FWHM (x, y, z) | FWHM _{x, y, z} | (1.2784, 0.6936, 0.6936) mm |
| Peak density | n_0 | $(1.46 \pm 0.14) \times 10^{10} \text{ cm}^{-3}$ |
| Free fit (base-10 logs) | m, b | $m = 2.046 \pm 0.036, b = -0.313 \pm 0.031$ |
| Fitted rate prefactor (corrected) | α_{corr} | $2.60 \times 10^{11} \text{ s}^{-1} \text{ W}^{-2}$ |
| Two-photon cross-section | δ | $(6.92 \pm 1.38) \times 10^{-39} \text{ cm}^4 \cdot \text{s}/\text{photon}$ $(6.92 \pm 1.38) \times 10^{11} \text{ GM}$ |

APPENDIX E. ALLAN DEVIATION BENCHMARKS

Allan deviation measurements, originally conceived during the development of the optical clock [67], is a way of benchmarking experimental stability when taking long-term measurements. In past work [26], we have used the Allan deviation to benchmark our experiments. Since in this paper we collect data over extended periods, we performed Allan deviation analysis to ensure statistical robustness. With the trap and repump beams on and the optical chopper cycling, Allan deviation of the detector (during the off cycle) begins to show deviations from linearity on the order of 1.0×10^4 - 1.5×10^4 seconds, setting the maximum collection time used.

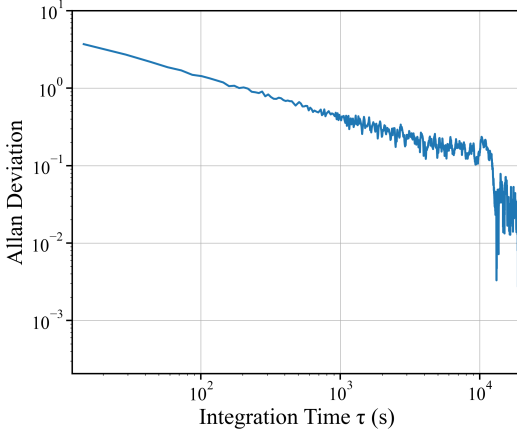


FIG. 7. Allan deviation of the detector with trap and cooling beams engaged (the time-gated two-photon component with the trap and repump beams blocked was analyzed). The Allan deviation continues to decrease linearly until the $1 - 1.5 \times 10^4$ second range, beyond which indicates that longer experimental collections cannot yield improved statistical outcomes.

APPENDIX F. TWO-PHOTON LOG-LOG PLOTS OF POWER DEPENDENCE

The following figure shows the two-photon log-log plots in terms for laser power (instead of flux). The laser power in μW is reported above each datapoint for ease of visualization. Using statistical analysis, the lowest significant powers were $1.01 \mu\text{W}$ for ^{85}Rb and $1.21 \mu\text{W}$ for ^{87}Rb .

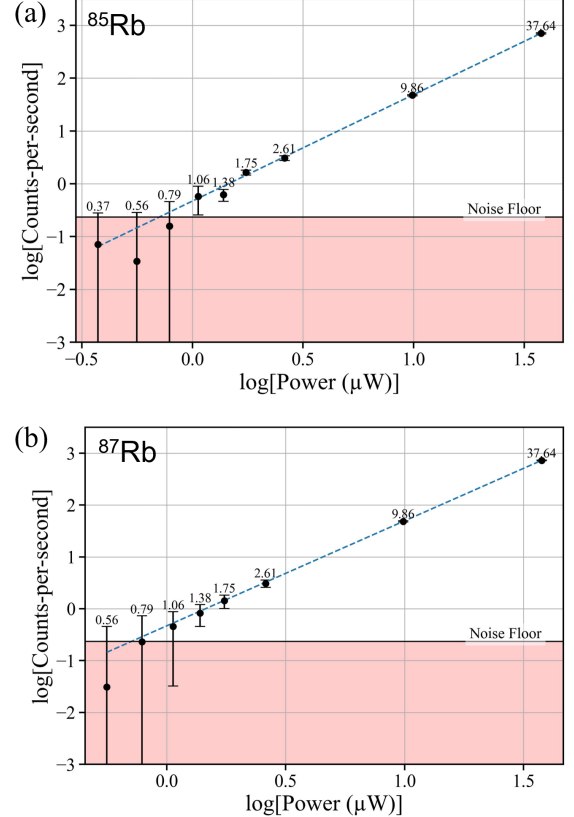


FIG. 8. Two-photon log-log plot with counts as a function of power. (a) Two-photon power dependence of ^{85}Rb . (b) Two-photon power dependence of ^{87}Rb .

APPENDIX G. FLUORESCENCE COLLECTION EFFICIENCY

A determination of the fluorescence collection efficiency (CE) of our system was necessary (for example, CE is required to determine the TPA cross-section). However, characterizing the MOT fluorescence collection through use of the MOT's own fluorescence has challenges. A one-photon fluorescence signal is not possible to deconvolute from MOT beam scatter and excitation beam scatter. Therefore, we determined the collection efficiency computationally using Zemax. Zemax is a software package that allows the spatial modeling of an optics system in a CAD-like environment, utilizing source, detection, optical, and passive objects [68]. Light propagation is modeled using ray tracing or wave propagation methods, with the ray tracing option providing fast results for macroscopic optical systems [68]. Components such as the cell walls, coil arms and coil housings are included in our model, Figure 9A. Given physical constraints due to the Rb cell and coils of the MiniMOT V2, Zemax was useful in selecting compatible optics and optimizing their positioning. Before settling on final components, manufacturer-supplied Zemax models were explored for various commercial optics. At the end, we selected a 38.4 mm diameter collimating lens because this was the largest lens that fit in the enclosure to maximize ray solid angle.

To perform the characterization, optics elements were downloaded and imported into the Zemax software in non-sequential mode. The fluorescence source was modeled using a source point object, 10^3 rays were used for the display (Figure 9A) and 10^6 rays were used for the computation. The detector was simulated by creating a 2D detector surface object of minimum aperture 4.0 mm radius (matching the experimental detector size of 8 mm on the Hamamatsu PMT). Maximum collection efficiency was 16.1% (determined by dividing the total hits on the detector by the input number rays of 10^6), Figure 9B. Lens 1 and lens 2 are experimentally coupled translationally. Varying their offset in Zemax showed that collection efficiency is sensitive on the mm scale, but micron-level offsets (controllable using micrometers) allow the maximum collection efficiency to easily be attained as shown in Figure 9B. Similarly, in Figure 9C, the location of the fluorescent point source was varied (with the experimentally measured value set to 0). Though spatial sensitivity does exist, offsets up to the range of approximately 2 mm retain collection efficiency within 80% of the maximum (of far greater magnitude than the experimentally controllable offset).

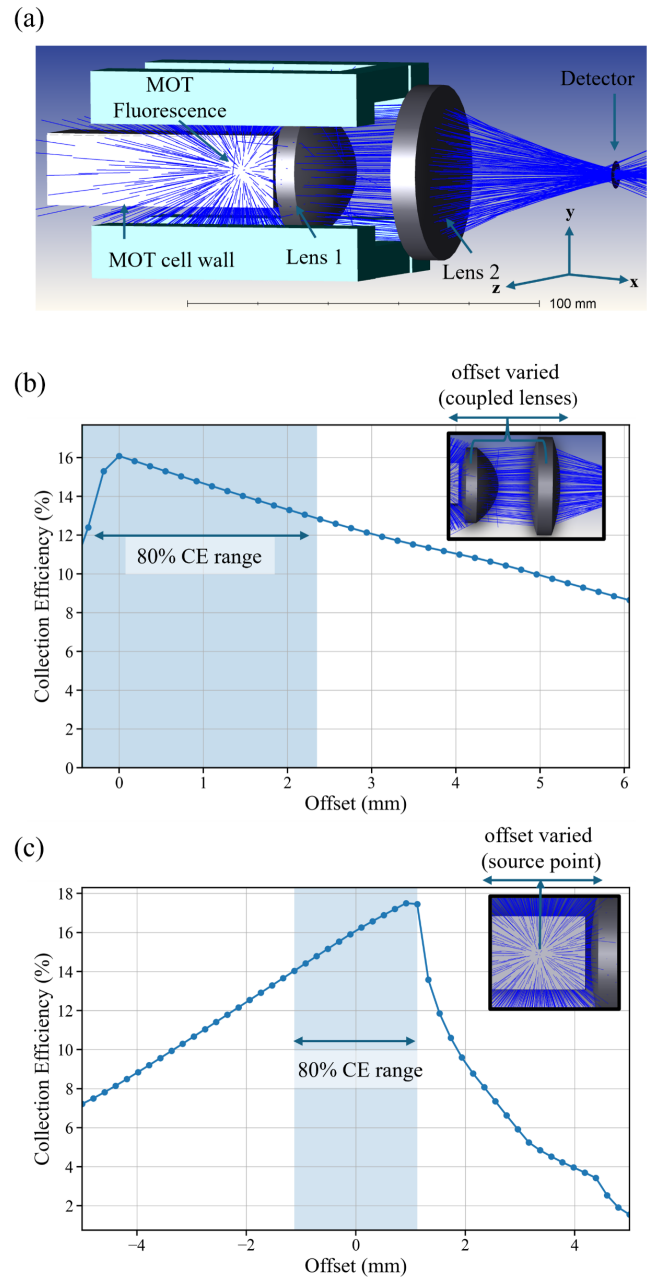


FIG. 9. (a) Overview of the lens system (source point, lenses, detector, and MOT apparatus) used to collect TPEF from Rb, (b) Collection efficiency (%) versus the offset of the 2-lens doublet (the distance between the 2-lenses in the doublet is fixed to the experimental value). With optimal alignment, 16.1% fluorescence collection efficiency is achieved. The region of 80% collection efficiency from the maximum is shown in blue. (c) Collection efficiency (%) versus the source point offset (0 mm is the measured MOT position). The region of 80% collection efficiency from the maximum is shown in blue. For (b) and (c) figures the detector position is fixed at the experimental value.

APPENDIX H. REPORTED MOT DENSITIES

This Appendix includes densities that were achieved using Rb MOTs. The MOTs are divided into three categories, 1. Standard MOTs (no extra techniques), 2. Standard MOTs with extra techniques (such as using multiple trapping lasers with different detunings), 3. Sub-Doppler cooled MOTs (including dark MOTs and polarization-gradient detuning).

TABLE V. Representative $^{85/87}\text{Rb}$ MOT peak densities across regimes. “Standard” refers to Doppler-limited MOTs with no compression or sub-Doppler cooling [69–71]. “Bright/Compressed” includes higher-gradient or CMOT techniques (no sub-Doppler) [72, 73]. “Sub-Doppler / Dark-State” MOTs employ gray or blue-detuned cooling for enhanced densities [39, 73, 74].

| Reference | Isotope | Method / Regime | Peak Density (cm^{-3}) |
|------------------------------------|------------------|----------------------------------------------|---------------------------------------------------|
| <i>Standard Rb MOTs</i> | | | |
| Cahpovsky et al. [69] | ^{85}Rb | Standard (small diameter beams) | $\sim 7 \times 10^{10}$ |
| Menegatti et al. [70] | ^{87}Rb | Standard | $\sim 2 \times 10^{10}$ |
| Isichenko et al. [†] [71] | ^{87}Rb | Standard (Inflection miniMOT) | $\sim 4.8 \times 10^{10}$ |
| <i>Bright/Compressed MOTs</i> | | | |
| Sinclair et al. [72] | ^{85}Rb | Standard with multi-frequency & center block | $\sim 2.2 \times 10^{11}$ |
| Jarvis et al. [73] | ^{87}Rb | Compressed MOT | up to 5×10^{11} |
| <i>Sub-Doppler/Dark-State MOTs</i> | | | |
| Radwell et al. [74] | ^{87}Rb | Dark-spot MOT | up to $> 10^{12}$ |
| Hoekstra et al. [39] | ^{85}Rb | Temporal dark MOT | $1.6 \times 10^{10} \rightarrow 6 \times 10^{10}$ |
| Jarvis et al. [73] | ^{87}Rb | Blue-detuned type II MOT | $> 10^{11}$ |

Notes: [†] Deduced from $N \approx 1.3 \times 10^6$ atoms and a 3D Gaussian cloud with $1/e^2$ diameter 0.48 mm ($w = 0.24$ mm). Using $n_0 = N(2/\pi)^{3/2}/(w_x w_y w_z)$ with $w_x = w_y = w_z$ gives $n_0 \approx 4.8 \times 10^{10} \text{ cm}^{-3}$ [71].

APPENDIX I. LINENWIDTH BROADENING

This appendix contains linewidth broadening calculations for ^{85}Rb and ^{87}Rb .

To calculate the Doppler broadening, we assume that the MOT has obtained the Doppler limit of $145.57 \mu\text{K}$, which is identical for ^{85}Rb and ^{87}Rb [75, 76]. We then find the Doppler broadening:

$$\Delta\nu_D = 2\nu_0 \sqrt{\frac{2k_B T \ln(2)}{mc^2}} \quad (\text{I1})$$

To find the magnetic broadening, we consider the “anomalous” Zeeman splitting energies

$$\Delta E = g_J \mu_B B \quad (\text{I2})$$

where μ_B is the Bohr magneton, g_J is the Landé g factor, and B is the strength of the magnetic field. To find the maximum broadening, we consider the maximum field strength given the gradient of 14 G/cm (based on the miniMOT specs for the 1A current that is run) and assume excitation only happens within the Rayleigh length of $2w_0$. This is noted as the Zeeman broadening in Table VI. We use this same equation to find the broadening from the finite local field in the MOT, which our calculation determines to be 0.13 G . This value is reasonable in the absence of using correction gradients to shim the MOT center. This broadening is treated separately and is noted as local field broadening in Table VI.

Pressure broadening was calculated using the standard formula of

$$\Delta\nu_P = bp \quad (\text{I3})$$

where b is an experimentally determined coefficient. For ^{85}Rb and ^{87}Rb , it has a value of $(10 \pm 1) \text{ MHz/Torr}$ [77].

Power broadening was estimated using the time-energy uncertainty equation

$$\Delta E \Delta t \geq \hbar \quad (\text{I4})$$

from which the estimate of

$$\Delta\nu \sim \frac{\mu E}{2\pi\hbar} \quad (\text{I5})$$

can be derived, where E is the electric field strength and μ is the dipole transition moment. These calculations used reduced matrix elements [78] to provide an approximate upper bound on the magnitude of the broadening for the highest reported power of $37 \mu\text{W}$.

The results of these calculations are found in Table VI. The total broadening includes the natural lifetime broadening of the transition and makes the standard assumption that broadenings add in quadrature [79].

TABLE VI. Linewidth broadening calculations for Zeeman, Doppler, Local field, and Power broadening mechanisms factoring into account parameters from our experiment.

| Broadening Type | ^{85}Rb | ^{87}Rb |
|------------------------------|------------------|------------------|
| Lifetime Broadening (kHz) | 660 | 660 |
| Zeeman Broadening (kHz) | 180 | 180 |
| Local field Broadening (kHz) | 1300 | 1300 |
| Doppler Broadening (kHz) | 360 | 370 |
| Pressure Broadening (Hz) | < 1 | < 1 |
| Power Broadening (kHz) | 450 | 450 |
| Total Broadening (MHz) | 1.58 | 1.58 |

[1] K. W. Martin, G. Phelps, N. D. Lemke, M. S. Bigelow, B. Stuhl, M. Wojcik, M. Holt, I. Coddington, M. W. Bishop, and J. H. Burke, Compact optical atomic clock based on a two-photon transition in rubidium, *Phys. Rev. Appl.* **9**, 014019 (2018).

[2] C.-H. Chu, P.-C. Chang, Y.-J. Shih, D.-A. Luh, M.-S. Chang, T.-W. Liu, Y.-T. Lin, B.-W. Chen, and W.-Y. Cheng, Measurement of the $5s_{1/2} \rightarrow 5d_{5/2}$ two-photon clock transition frequency of rubidium-85 in high vacuum, *Opt. Lett.* **48**, 5984 (2023).

[3] J. Leng, H. Xu, H. Lu, Y. Fan, and J. Zhao, Optical communication frequency standard using a fiber laser to excite cold rubidium two-photon transition, *J. Opt. Soc. Am. B* **36**, 1183 (2019).

[4] H. Lu, J. Leng, and J. Zhao, The optimization of cold rubidium atom two-photon transition excitation with an erbium-fiber optical frequency comb, *Appl. Sci.* **9**, 921 (2019).

[5] M. Carey, M. Belal, M. Himsworth, J. Bateman, and T. Freegarde, Matterwave interferometric velocimetry of cold rb atoms, *J. Mod. Opt.* **65**, 657 (2018).

[6] G. P. Greve, C. Luo, B. Wu, and J. K. Thompson, Entanglement-enhanced matter-wave interferometry in a high-finesse cavity, *Nature* **610**, 472 (2022).

[7] Q.-Q. Hu, C. Freier, B. Leykauf, V. Schkolnik, J. Yang, M. Krutzik, and A. Peters, Mapping the absolute magnetic field and evaluating the quadratic zeeman effect induced systematic error in an atom interferometer gravimeter, *Phys. Rev. A* **96**, 033414 (2017).

[8] M. Schmidt, A. Senger, M. Hauth, C. Freier, V. Schkolnik, and A. Peters, A mobile high-precision absolute gravimeter based on atom interferometry, *Gyroscopy and Navigation* **2**, 170 (2011).

[9] C. Chen, G. Bornet, M. Bintz, G. Emperaiger, L. Leclerc, V. S. Liu, P. Scholl, D. Barredo, J. Hauschild, S. Chatterjee, M. Schuler, A. M. Läuchli, M. P. Zaletel, T. Lahaye, N. Y. Yao, and A. Browaeys, Continuous symmetry breaking in a two-dimensional rydberg array, *Nature* **616**, 691 (2023).

[10] C. Luo, H. Zhang, A. Chu, R. Maruko, A. M. Rey, and J. K. Thompson, Hamiltonian engineering of collective xyz spin models in an optical cavity, *Nature Physics* **21**, 916 (2025).

[11] D. Bluvstein, S. J. Evered, A. A. Geim, S. H. Li, H. Zhou, T. Manovitz, S. Ebadi, M. Cain, M. Kalinowski, D. Hangleiter, J. P. B. Ataides, N. Maskara, I. Cong, X. Gao, P. S. Rodriguez, T. Karolyshyn, G. Semeghini, M. J. Gullans, M. Greiner, V. Vuletić, and M. D. Lukin, Logical quantum processor based on reconfigurable atom arrays, *Nature* **626**, 58 (2023).

[12] C. Drago, A. McLean, R. Jimenez, and J. Sipe, Two-photon absorption of squeezed light by rubidium atoms: Will Doppler do us in?, *CLEO: Fundamental Science*, JTh2A-5, 2023.

[13] M. Caracas Núñez, M. A. Gonzalez, and M. Núñez Portela, Theoretical and experimental study of the 6S-8S two-photon absorption cross-section in cesium atoms, *Opt. Express* **31**, 31749 (2023).

[14] C. Drago and J. E. Sipe, Fluorescence driven by nonclassical light, *arXiv preprint arXiv:2508.12037* (2025).

[15] M. Rubart, Two-photon microscopy of cells and tissue, *Circ. Res.* **95**, 1154 (2004).

[16] F. Helmchen and W. Denk, Deep tissue two-photon microscopy, *Nat. Methods* **2**, 932 (2005).

[17] J. Bhawalkar, N. Kumar, C.-F. Zhao, and P. Prasad, Two-photon photodynamic therapy, *J. Clin. Laser Med. Surg.* **15**, 201 (1997).

[18] D. Tabakaev, M. Montagnese, G. Haack, L. Bonacina, J.-P. Wolf, H. Zbinden, and R. T. Thew, Energy-time-entangled two-photon molecular absorption, *Phys. Rev. A* **103**, 033701 (2021).

[19] D. Tabakaev, A. Djorović, L. La Volpe, G. Gaulier, S. Ghosh, L. Bonacina, J.-P. Wolf, H. Zbinden, and R. Thew, Spatial properties of entangled two-photon absorption, *Phys. Rev. Lett.* **129**, 183601 (2022).

[20] J. P. Villabona-Monsalve, O. Varnavski, B. A. Palfey, and T. Goodson III, Two-photon excitation of flavins and flavoproteins with classical and quantum light, *J. Am. Chem. Soc.* **140**, 14562 (2018).

[21] T. Li, F. Li, C. Altuzarra, A. Classen, and G. S. Agarwal, Squeezed light induced two-photon absorption fluorescence of fluorescein biomarkers, *Appl. Phys. Lett.* **116**, 254001 (2020).

[22] J. P. Villabona-Monsalve, O. Calderón-Losada, M. Nuñez Portela, and A. Valencia, Entangled two photon absorption cross section on the 808 nm region for the common dyes zinc tetraphenylporphyrin and rhodamine B, *J. Phys. Chem. A* **121**, 7869 (2017).

[23] O. Varnavski, B. Pinsky, and T. Goodson III, Entangled photon excited fluorescence in organic materials: an ultrafast coincidence detector, *J. Phys. Chem. Lett.* **8**, 388 (2017).

[24] O. Varnavski and T. Goodson III, Two-photon fluorescence microscopy at extremely low excitation intensity: The power of quantum correlations, *J. Am. Chem. Soc.* **142**, 12966 (2020).

[25] O. Varnavski, C. Gunthardt, A. Rehman, G. D. Luker, and T. Goodson III, Quantum light-enhanced two-photon imaging of breast cancer cells, *J. Phys. Chem. Lett.* **13**, 2772 (2022).

[26] K. M. Parzuchowski, A. Mikhaylov, M. D. Mazurek, R. N. Wilson, D. J. Lum, T. Gerrits, C. H. Camp, M. J. Stevens, and R. Jimenez, Setting experimental bounds on entangled two-photon absorption cross sections, *Phys. Rev. Appl.* **15**, 044012 (2021).

[27] T. Landes, B. J. Smith, and M. G. Raymer, Limitations in fluorescence-detected entangled two-photon-absorption experiments: Exploring the low-to high-gain squeezing regimes, *Phys. Rev. A* **110**, 033708 (2024).

[28] M. G. Raymer, T. Landes, M. Allgaier, S. Merkouche, B. J. Smith, and A. H. Marcus, How large is the quantum enhancement of two-photon absorption by time-frequency entanglement of photon pairs?, *Optica* **8**, 757 (2021).

[29] A. Mikhaylov, R. N. Wilson, K. M. Parzuchowski, M. D. Mazurek, C. H. J. Camp, M. J. Stevens, and R. Jimenez, Hot-band absorption can mimic entangled two-photon absorption, *J. Phys. Chem. Lett.* **13**, 1489 (2022).

[30] B. P. Hickam, M. He, N. Harper, S. Szoke, and S. K. Cushing, Single-photon scattering can account for the discrepancies among entangled two-photon measurement techniques, *J. Phys. Chem. Lett.* **13**, 4934 (2022).

[31] S.-Y. Baek and Y.-H. Kim, Spectral properties of entan-

gled photons generated via type-I spontaneous parametric down-conversion, *Phys. Rev. A* **80**, 033814 (2009).

[32] B. Farella, G. Medwig, R. A. Abrahao, and A. Nomerotski, Spectral characterization of an SPDC source with a fast broadband spectrometer, *AIP Adv.* **14**, 045034 (2024).

[33] D. Sheng, A. Perez Galvan, and L. A. Orozco, Lifetime measurements of the $5d$ states of rubidium, *Phys. Rev. A* **78**, 062506 (2008).

[34] N. P. Georgiades, Nonclassical excitation and quantum interference in a three level atom, PhD thesis, California Institute of Technology, Pasadena, California (1998).

[35] K. M. Parzuchowski, Setting experimental bounds on entangled two-photon absorption cross sections, PhD thesis, University of Colorado Boulder (2023).

[36] C. Xu and W. W. Webb, Measurement of two-photon excitation cross sections of molecular fluorophores with data from 690 to 1050 nm, *J. Opt. Soc. Am. B* **13**, 481 (1996).

[37] K. Saha, V. Venkataraman, P. Londero, and A. L. Gaeta, Enhanced two-photon absorption in a hollow-core photonic-band-gap fiber, *Phys. Rev. A* **83**, 033833 (2011).

[38] W. Zapka, M. D. Levenson, F. M. Schellenberg, A. C. Tam, and G. C. Bjorklund, Continuous-wave Doppler-free two-photon frequency-modulation spectroscopy in rb vapor, *Opt. Lett.* **8**, 27 (1983).

[39] B. Hoekstra, High-density trapping of rubidium-85 with a temporal dark magneto-optical trap, Master's thesis, Eindhoven University of Technology (2017).

[40] G. Reinaudi, T. Lahaye, Z. Wang, and D. Guéry-Odelin, Strong saturation absorption imaging of dense clouds of ultracold atoms, *Opt. Lett.* **32**, 3143 (2007).

[41] K. Hueck, N. Luick, L. Sobirey, J. Siegl, T. Lompe, and H. Moritz, Calibrating high intensity absorption imaging of ultracold atoms, *Opt. Express* **25**, 8670 (2017).

[42] E. L. Raab, M. Prentiss, A. Cable, S. Chu, and D. E. Pritchard, Trapping of neutral sodium atoms with radiation pressure, *Phys. Rev. Lett.* **59**, 2631 (1987).

[43] A. J. Olson, E. J. Carlson, and S. K. Mayer, Two-photon spectroscopy of rubidium using a grating-feedback diode laser, *Am. J. Phys.* **74**, 218 (2006).

[44] C. L. A. Collins, K. D. Bonin, and M. A. Kadar-Kallen, Absolute two-photon cross section of Rb measured by differential absorption, *Opt. Lett.* **18**, 1754 (1993).

[45] K. Hassanin, P. Federsel, F. Karlewski, and C. Zimmermann, 5S-5D two-photon transition in rubidium vapor at high densities, *Phys. Rev. A* **107**, 043104 (2023).

[46] K. M. Parzuchowski, M. D. Mazurek, C. H. J. Camp, M. J. Stevens, and R. Jimenez, A liquid-core fiber platform for classical and entangled two-photon absorption measurements, *ACS Photonics* **12**, 1470 (2025).

[47] J. A. Rushton, M. Aldous, and M. D. Himsouth, The feasibility of a fully miniaturized magneto-optical trap for portable ultracold quantum technology, *Rev. Sci. Instrum.* **85**, 121501 (2014).

[48] D. Pizzey, J. Briscoe, F. Logue, F. Ponciano-Ojeda, S. Wrathmall, and I. Hughes, Laser spectroscopy of hot atomic vapours: from 'scope to theoretical fit, *New J. Phys.* **24**, 125001 (2022).

[49] O. Terra and H. Hussein, An ultra-stable optical frequency standard for telecommunication purposes based upon the $5s_{1/2} \rightarrow 5d_{5/2}$ two-photon transition in rubidium, *Appl. Phys. B* **74**, 218 (2009).

[50] R. E. Ryan, L. A. Westling, and H. J. Metcalf, Two-photon spectroscopy in rubidium with a diode laser, *J. Opt. Soc. Am. B* **10**, 1643 (1993).

[51] SABIC Innovative Plastics, *ULTEM® 1000 Polyetherimide (PEI) Resin Datasheet* (2024).

[52] U. Schünemann, H. Engler, R. Grimm, M. Weidemüller, and M. Zielonkowski, Simple scheme for tunable frequency offset locking of two lasers, *Rev. Sci. Instrum.* **70**, 242–243 (1999).

[53] K. Luksch, Measurement of the number of atoms in a magneto-optical trap using absorption imaging, *Diss. Diploma thesis*, National University of Singapore (2012).

[54] W. DeGraffenreid and C. J. Sansonetti, $2^2s_{1/2}\beta4^2s_{1/2}$ transition of atomic lithium by Doppler-free two-photon spectroscopy, *Phys. Rev. A* **67**, 012509 (2003).

[55] W. DeGraffenreid and C. J. Sansonetti, Foreign gas pressure broadening and shifts of the $2s-4s$ two-photon transition of atomic lithium, *J. Phys. B* **36**, 2099 (2003).

[56] G. C. Tisone and P. J. Hargis Jr., Laser absorption and fluorescence studies of the lithium $2s-3d$ transition, *AIP Conf. Proc.*, 1987.

[57] I. Labazan and S. Milošević, Lithium vapour excitation at $2s \rightarrow 3d$ two-photon resonance, *Eur. Phys. J. D* **8**, 41 (2000).

[58] M. D. Levenson and N. Bloembergen, Observation of two-photon absorption without Doppler Broadening on the $3s-5s$ transition in sodium vapor, *Phys. Rev. Lett.* **32**, 645 (1974).

[59] T. W. Hänsch, K. C. Harvey, G. Meisel, and A. L. Schawlow, Two-photon spectroscopy of Na $3s-4d$ without Doppler Broadening using a CW dye laser, *Opt. Commun.* **11**, 50 (1974).

[60] Y.-W. Liu and P. E. G. Baird, Two-photon spectroscopy in potassium, *Meas. Sci. Technol.* **12**, 740 (2001).

[61] M.-S. Ko and Y.-W. Liu, Observation of rubidium $5s_{1/2} \rightarrow 7s_{1/2}$ two-photon transitions with a diode laser, *Opt. Lett.* **29**, 1799 (2004).

[62] P. Morzyński, P. Wcisło, P. Ablewski, R. Gartman, W. Gawlik, P. Masłowski, B. Nagórny, F. Ozimek, C. Radzewicz, M. Witkowski, R. Ciuryło, and M. Zawada, Absolute frequency measurement of rubidium $5s-7s$ two-photon transitions, *Opt. Lett.* **38**, 4581 (2013).

[63] S. Wang, J. Yuan, L. Wang, L. Xiao, and S. Jia, A stable frequency standard based on the one-color two-photon $5s_{1/2}-7s_{1/2}$ transition in rubidium vapor, *Opt. Express* **27**, 6528 (2019).

[64] N. P. Georgiades, E. S. Polzik, and H. J. Kimble, Two-photon spectroscopy of the $6s_{1/2} \rightarrow 6d_{5/2}$ transition of trapped atomic cesium, *Opt. Lett.* **19**, 1474 (1994).

[65] V. A. Sautenkov, S. A. Saakyan, E. V. Vilshanskaya, B. B. Zelener, and B. V. Zelener, Power broadening of two-photon coherent resonances on rydberg atomic transitions in a magneto-optical trap, *J. Russ. Laser Res.* **38**, 91 (2017).

[66] V. A. Sautenkov, S. A. Saakyan, A. A. Bobrov, E. V. Vilshanskaya, B. B. Zelener, and B. V. Zelener, Differential two-photon spectroscopy for nondestructive temperature measurements of cold light atoms in a magneto-optical trap, *J. Opt. Soc. Am. B* **35**, 1546 (2018).

[67] D. W. Allan, Statistics of atomic frequency standards, *Proc. IEEE* **54**, 221 (1966).

[68] *Zemax OpticStudio User Manual*, Zemax LLC (2022).

[69] P. L. Chapovsky, Compact magneto-optical trap for rubidium atoms, *J. Exp. Theor. Phys.* **100**, 911 (2005).

[70] C. R. Menegatti, B. S. Marangoni, N. Bouloufa-Maafa, O. Dulieu, and L. G. Marcassa, Trap loss in a rubidium

crossed dipole trap by short-range photoassociation, *Phys. Rev. A* **87**, 053404 (2013).

[71] A. Isichenko, N. Chauhan, D. Bose, J. Wang, P. D. Kunz, and D. J. Blumenthal, Photonic integrated beam delivery for a rubidium 3d magneto-optical trap, *Nat. Commun.* **14**, 3080 (2023).

[72] A. G. Sinclair, E. Riis, and M. J. Snadden, Improved trapping in a vapor-cell magneto-optical trap with multiple laser frequencies, *J. Opt. Soc. Am. B* **11**, 2333 (1994).

[73] K. N. Jarvis, J. A. Devlin, T. E. Wall, B. E. Sauer, and M. R. Tarbutt, Blue-detuned magneto-optical trap, *Phys. Rev. Lett.* **120**, 083201 (2018).

[74] N. Radwell, G. Walker, and S. Franke-Arnold, Cold-atom densities of more than 10^{12} cm $^{-3}$ in a holographically shaped dark spontaneous-force optical trap, *Phys. Rev. A* **88**, 043409 (2013).

[75] D. A. Steck, Rubidium 85 D Line Data (2003–2026).

[76] D. A. Steck, Rubidium 87 D Line Data (2003–2026).

[77] A. Sargsyan, T. Vartanyan, and D. Sarkisyan, Broadening and shift of the D1 and D2 lines of Rb atoms by neon: Resolving hyperfine components in a half-wave cell using double differentiation with respect to frequency, *Opt. Spectrosc.* **129**, 1173– (2021).

[78] H. Eicher, Third-order susceptibility of alkali metal vapors, *IEEE J. Quantum Electron.* **11**, 121 (1975).

[79] G.-W. Truong, D. A. Long, A. Cygan, D. Lisak, R. D. van Zee, and J. T. Hedges, Comb-linked, cavity ring-down spectroscopy for measurements of molecular transition frequencies at the kHz-level, *J. Chem. Phys.* **138** (2013).